

# Geometrically manipulating photonic Schrödinger cat states and realizing cavity phase gates

Y. Xu,<sup>1</sup> W. Cai,<sup>1</sup> Y. Ma,<sup>1</sup> X. Mu,<sup>1</sup> W. Dai,<sup>1</sup> W. Wang,<sup>1</sup> L. Hu,<sup>1</sup> X. Li,<sup>1</sup> J. Han,<sup>1</sup>  
H. Wang,<sup>1</sup> Y. P. Song,<sup>1</sup> Zhen-Biao Yang,<sup>2,\*</sup> Shi-Biao Zheng,<sup>2,†</sup> and L. Sun<sup>1,‡</sup>

<sup>1</sup>*Center for Quantum Information, Institute for Interdisciplinary Information Sciences, Tsinghua University, Beijing 100084, China*

<sup>2</sup>*Fujian Key Laboratory of Quantum Information and Quantum Optics,  
College of Physics and Information Engineering, Fuzhou University, Fuzhou, Fujian 350116, China*

Schrödinger cat states are crucial for exploration of fundamental issues of quantum mechanics and have important applications in quantum information processing. Here, we propose and experimentally demonstrate a method for manipulating cat states in a cavity with the Aharonov-Anandan phase acquired by a superconducting qubit, which is dispersively coupled to the cavity. Based on this dispersive coupling, the qubit can be forced to trace out a circuit in the projective Hilbert space conditional on one coherent state. By preparing the cavity in a superposition of two coherent states, the geometric phase associated with this transport is encoded to the relative probability amplitude of these two coherent states. We demonstrate the photon-number parity of a cat state in a cavity can be controlled by adjusting this geometric phase, which offers the possibility for protecting its quantum coherence from single-photon loss. Based on this geometric effect, we realize phase gates for one and two photonic qubits whose logical basis states are encoded in two quasi-orthogonal coherent states. We further demonstrate two-cavity gates with symmetric and asymmetric Fock state encoding schemes. Our method can be directly extended to implementation of controlled-phase gates between error-correctable logical qubits.

When a quantum system is parallel-transported along a circuit in its quantum state space, it collects information about the geometry of this path, acquiring a “memory” of its motion in the form of a phase. This phase is referred to as the geometric phase and has close relations to many physical phenomena [1, 2]. This effect was first discovered by Berry in the context of adiabatic passage [3]. One remarkable feature of Berry phase is that it is robust against fast parameter fluctuations whose effect on the enclosed parameter-space area averages out [4]. As such, Berry phase has been considered as a choice for fault-tolerant quantum computation [5, 6]. So far, observation of this phase and demonstration of its noise-resilient feature have been reported in various physical systems [6–11]. Berry’s discovery has triggered considerable interest in quantum-mechanical geometric effects, leading to important generalizations in various directions [12, 13]. In particular, Aharonov and Anandan defined geometric phase in the projective Hilbert space, instead of in parameter space [12], removing the adiabatic condition. The geometric nature of Aharonov-Anandan (AA) phase lies in the fact that it is related to the area enclosed by the circuit traversed by the state vector.

When two or more quantum systems are coupled, the geometric phase acquired by one system can be employed to manipulate the quantum state of the others [10, 14]. The geometric phase of a harmonic vibrational mode of trapped ions has been utilized for implementing high-fidelity entangling gates for the ionic qubits [15]. In a recent experiment [16], the geometric phase of a continuous-variable field mode was observed through Ramsey interference and used for realizing controlled phase gates with up to four qubits in a superconducting circuit. On the other hand, it has been shown that the geometric phase of a superconducting qubit can be used for realizing Selective Number-dependent Arbitrary Phase (SNAP) gates on a cavity [17]. This kind of gates has been experimentally demonstrated and used to produce a single-photon

state [18]. Recently, a quantum controlled-NOT (CNOT) gate between two cavity systems has been demonstrated by use of both the dynamical and AA phases produced by controllably coupling these cavities to a qubit [19]. This gate requires the logic states of the control qubit to be respectively encoded on the vacuum state and a nonzero photon-number state, which renders it incompatible with quantum error correction schemes; on the occurrence of single-photon loss the control qubit will collapse to a Fock state, leading to complete loss of the stored information.

We here propose and experimentally demonstrate a scheme for manipulating the parity of a cat state in a cavity with the AA phase of a qubit dispersively coupled to the cavity in a superconducting circuit. Cat states are of fundamental interest [20] and can be used to encode error-correctable logical qubits [21–24]. Thus, manipulating these states and protecting them from decoherence is a subject of great importance. In our experiment, the qubit is parallel-transported along a closed loop on the Bloch sphere, picking up a geometric phase, conditional on one of the two quasiclassical components forming the cat state. We demonstrate the photon-number parity of the cat state can be manipulated by this geometric operation. This manipulation technique, in combination with the parity jump tracking method [25], allows for the protection of the quantum coherence of cat states from single-photon loss. We then employ this phase to realize logic gates for a cat-encoded qubit, and generalize our method to implementation of two-cavity controlled-phase gates with different encoding schemes and two-cavity SNAP gates for entangling two cavities. Our procedure can be directly generalized to implement gates between logic qubits with inherent error correction function.

The experiments presented in this work are based on two circuit quantum electrodynamics (QED) devices [26–30]. Device A, on which single-cavity geometric phase gates are performed, consists of two transmon qubits simultaneously dispersively coupled to two three-dimensional cavities [31–

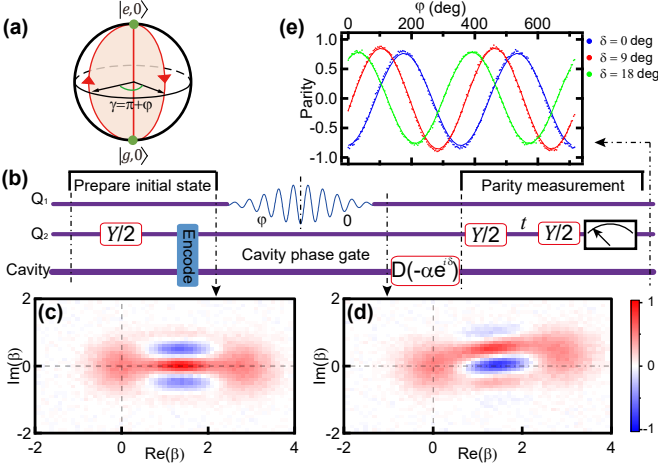


FIG. 1: Geometric manipulation of a photonic cat state. (a) Schematic of the nonadiabatic AA phase of a qubit. Two successive  $\pi$  rotations of the qubit produce a geometric phase  $\gamma = \pi + \phi$ , where  $\phi$  is the angle between the two rotation axes. (b) Experimental sequence to manipulate the cat state. A cavity is dispersively coupled to the qubit and initialized in a cat state  $(|0\rangle + |2\sqrt{2}\rangle)/\sqrt{2}$  with the help of an ancillary qubit  $Q_2$ . The AA phase produced by the rotations of  $Q_1$  conditional on the cavity's vacuum state is encoded in the probability amplitude of  $|0\rangle$ , resulting in a phase gate. (c) Measured Wigner function of the cavity state before the phase gate, corresponding to fidelity of 0.980 to the ideal cat state. (d) Wigner function of the cavity state after the gate with  $\phi = 0$ . The slight rotation and deformation of the Wigner function is due to the self-Kerr effect of the cavity. (e) Measured parity of the cavity state as a function of  $\phi$  after a displacement  $D(-\sqrt{2}e^{i\delta})$  for different values of  $\delta$ . Symbols are experimental data, in excellent agreement with numerical simulations (solid lines).

35]. The parameters and architecture setup are described in Ref. [36]. Device B, on which two-cavity geometric phase gates are performed, consists of three transmon qubits dispersively coupled to two cylindrical cavities [37] and three stripline readout cavities [38]. The device parameters are described in Ref. [39]. In Device A, the coupling between the qubit ( $Q_1$ ) used to produce the geometric phase and the cavity used to encode this phase is described by the Hamiltonian

$$H = -\hbar\chi_{qs}a^\dagger a|e\rangle\langle e|, \quad (1)$$

where  $\chi_{qs}$  denotes the qubit frequency shift induced by per photon,  $a^\dagger$  and  $a$  are the creation and annihilation operators for the particular cavity field respectively, and  $|e\rangle$  ( $|g\rangle$ ) is the excited (ground) state of the qubit. In Device B, the qubit, commonly coupled to two cavities used to store the photonic qubits, undergoes a frequency shift dependent on the photon numbers of both cavities.

The geometric manipulation technique is well exemplified with the even cat state  $(|\alpha\rangle + |-\alpha\rangle)/\sqrt{2}$ , where  $|\alpha\rangle$  and  $|-\alpha\rangle$  are coherent states with  $\langle\alpha|-\alpha\rangle \approx 0$ . To realize conditional qubit rotations, a phase-space displacement,  $D(\alpha)$ , is applied to the cavity, transforming its state to  $(|2\alpha\rangle + |0\rangle)/\sqrt{2}$ . The qubit, initially in the ground state  $|g\rangle$ , is then driven by a clas-

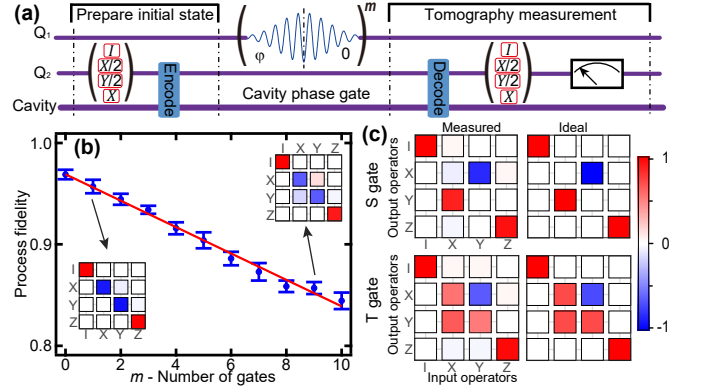


FIG. 2: Quantum process tomography of single-cavity geometric phase gates. (a) Experimental sequence. (b) The Pauli transfer process  $R$  matrix fidelity as a function of  $m$ , the number of the  $Z$  gate on the cavity state. The inserts show the measured  $R$  matrices after one and nine  $Z$  gates, respectively. A linear fit of the process fidelity decay gives the  $Z$  gate fidelity  $F_Z = 0.987 \pm 0.001$ . (c) The measured and ideal Pauli transfer  $R$  matrices of the S gate and T gate with fidelities  $F_S = 0.968$  and  $F_T = 0.964$ .

sical field on resonance with the qubit frequency conditioned on the cavity's vacuum state  $|0\rangle$ . We here assume that the Rabi frequency  $\varepsilon$  of the drive is much smaller than  $\bar{n}\chi_{qs}$ , where  $\bar{n}$  is the average photon number of the state  $|2\alpha\rangle$ . In this case, the qubit's state is not changed by the drive when the cavity is in  $|2\alpha\rangle$  due to the large detuning, and the system dynamics is described by the effective Hamiltonian

$$H_{\text{eff}} = \frac{1}{2}\hbar\varepsilon e^{i\phi}|e\rangle\langle g| \otimes |0\rangle\langle 0| + h.c., \quad (2)$$

where  $\phi$  is the phase of the drive. This Hamiltonian produces a qubit rotation  $R_{\mathbf{n}}^\theta$  conditional on the cavity's vacuum state, where  $R_{\mathbf{n}}^\theta$  represents the operation that rotates the qubit's state by an angle  $\theta = \int_0^\tau \varepsilon dt$  around the axis  $\mathbf{n}$  with an angle  $\phi$  to  $x$  axis on the equatorial plane of the Bloch sphere, with  $\tau$  being the pulse duration.

After two successive conditional  $\pi$  rotations  $R_{\mathbf{n}_1}^{\pi,0} = R_{\mathbf{n}_1}^\pi \otimes |0\rangle\langle 0|$  and  $R_{\mathbf{n}_2}^{\pi,0} = R_{\mathbf{n}_2}^\pi \otimes |0\rangle\langle 0|$ , the qubit makes a cyclic evolution, returning to the initial state  $|g\rangle$  but acquiring a phase  $\gamma = \pi + \Delta\phi = \Omega/2$ , where  $\Delta\phi = \phi_1 - \phi_2$  represents the angle between the two rotation axes, and  $\Omega$  is the solid angle subtended by the trajectory traversed by the qubit on the Bloch sphere, as shown in Fig. 1(a). This conditional phase shift is encoded in the probability amplitude of the state component  $|0\rangle$ , leading to the cavity state  $(|2\alpha\rangle + e^{i\gamma}|0\rangle)/\sqrt{2}$ . A subsequent displacement  $D(-\alpha)$  transforms the cavity to the state  $(|\alpha\rangle + e^{i\gamma}|-\alpha\rangle)/\sqrt{2}$ . Due to the quantum interference of the two superposed coherent state components  $|\alpha\rangle$  and  $|-\alpha\rangle$ , the cavity parity  $P$  exhibits a periodical oscillation when the geometric phase  $\gamma$  is varied:  $P = \cos\gamma$ . The procedure allows for manipulation of the parity of the cat state; when  $\gamma = \pi$ , the parity is reversed. This procedure is equivalent to a phase gate operation for the cavity qubit with  $|\alpha\rangle$  and  $|-\alpha\rangle$  acting as the logic basis states, and can be used to correct for the parity

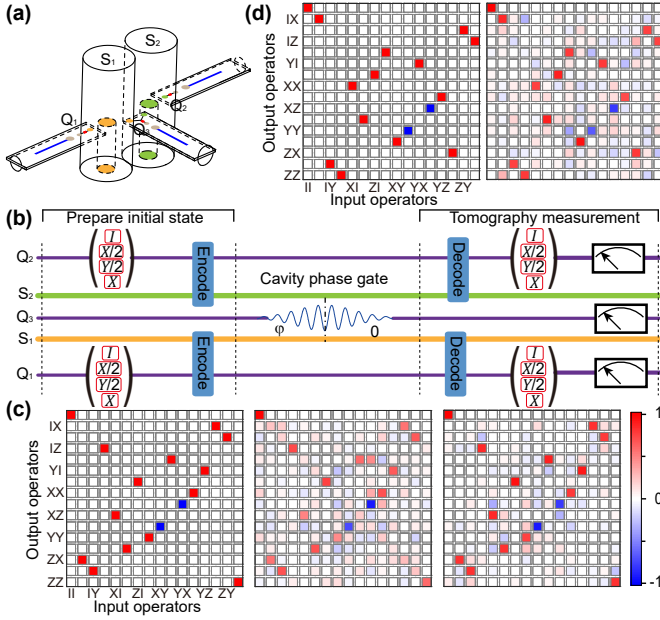


FIG. 3: Two-cavity geometric phase gate. (a) A 3D view of Device B. A superconducting transmon qubit  $Q_3$  at the center couples to two coaxial cavities  $S_1$  and  $S_2$ , which couple to two other individual ancillary transmon qubits  $Q_1$  and  $Q_2$ , respectively. Each of these transmon qubits independently couples to a stripline readout resonator used to perform simultaneous single-shot readout. (b) Schematic of the experimental sequence. (c) Ideal (left) and measured Pauli transfer  $R$  matrices of two-cavity CZ gates with coherent state encoding  $\{|0\rangle, |2\sqrt{2}\rangle\}$  (middle) and Fock state encoding  $\{|0\rangle, |1\rangle\}$  (right) for both cavities. The process fidelities,  $F_{CZ,ED}$  ( $F_{ED}$ ), for these two encodings are 0.727 (0.869) and 0.862 (0.905), respectively. (d) Ideal (left) and measured (right) Pauli transfer  $R$  matrices of the two-cavity CNOT gate with the encoding  $\{|0\rangle, |1\rangle\}$  for cavity  $S_1$  and  $\{|0\rangle_L = (|0\rangle + |2\rangle)/\sqrt{2}, |1\rangle_L = (|0\rangle - |2\rangle)/\sqrt{2}\}$  for cavity  $S_2$ . The corresponding process fidelity  $F_{CNOT,ED}$  ( $F_{ED}$ ) is 0.829 (0.857).

jump caused by single-photon loss.

To simplify the operation, in our experiment the cavity displacement before the conditional qubit rotation is incorporated with the preparation of the initial cavity state;  $|0\rangle$  and  $|2\alpha\rangle$  act as the two logic basis states for the gate demonstration. The experimental sequence to manipulate a cat state with Device A is shown in Fig. 1(b). The cavity is initialized in the cat state  $(|0\rangle + |2\sqrt{2}\rangle)/\sqrt{2}$  [the measured Wigner function is shown in Fig. 1(c)] with the help of ancillary qubit  $Q_2$  following the gradient ascent pulse engineering (GRAPE) technique [40, 41]. The two subsequent conditional  $\pi$  rotations on  $Q_1$ , with the first one around the axis with an angle  $\varphi$  to the  $x$  axis and the second one around the  $x$  axis, yield a geometric phase  $\gamma = \pi + \varphi$  conditional on the cavity's vacuum state. The Wigner function of the cavity state after this single-cavity geometric phase gate is shown in Fig. 1(d) with  $\varphi = 0$ , which demonstrates the phase-space interference fringes are reversed by the geometric manipulation. After a displacement  $D(-\sqrt{2}e^{i\delta})$ , the parity of the cavity state as a function of  $\varphi$  is measured and shown in Fig. 1(e), in excellent agreement with

numerical simulations.

Process tomography is used to benchmark the cavity geometric phase gate performance, with the experimental sequence shown in Fig. 2(a). Since trusted operations and measurements necessary for quantum process tomography are unavailable in the cat-encoded subspace, we characterize the gate by decoding the quantum information on the cavity back to the transmon qubit  $Q_2$ . We use the so-called Pauli transfer process  $R$  matrix as a measure of our gate [42], which connects the input and output Pauli operators with  $P_{out} = R \cdot P_{in}$ . Figure 2(b) shows the  $R$  matrix fidelity decay as a function of  $m$ , the number of the  $\pi$ -phase (Z) gate. The fidelity at  $m = 0$  quantifies the ‘‘round trip’’ process fidelity  $F_{ED} = 0.969$  of the encoding and decoding processes only. A linear fit of the process fidelity decay gives the Z gate fidelity  $F_Z = 0.987$ , also consistent with the fidelity calculated from  $F_Z = 1 - (F_{ED} - F_{Z,ED})$ , where  $F_{Z,ED} = 0.957$  is the measured fidelity including the encoding and decoding processes. The measured and the ideal Pauli transfer  $R$  matrices of the S gate and T gate are shown in Fig. 2(c), where  $S = |0\rangle_L \langle 0| + i|1\rangle_L \langle 1|$  and  $T = |0\rangle_L \langle 0| + \exp(i\pi/4)|1\rangle_L \langle 1|$ .

Our method can be directly generalized to implementation of controlled-phase gates between two photonic qubits encoded in two cavities that are dispersively coupled to one common superconducting qubit [43, 44]. The photon-number-dependent qubit frequency shift allows for the qubit  $2\pi$  rotation conditional on both cavities being in the vacuum state  $|00\rangle$  with a drive at the corresponding qubit frequency. With the encoding  $|0\rangle_L = |0\rangle$ , this rotation produces a  $\pi$ -phase shift if and only if both photonic qubits are in  $|0\rangle_L$ ; the other logic basis state of each qubit can be any nonzero photon-number state or a coherent state with a sufficiently large amplitude. If the two photonic basis states in each cavity correspond to two coherent states, the controlled-Z (CZ) gate can be achieved by sandwiching this conditional qubit rotation between two pairs of displacement operations: the first pair of displacements transform the coherent state of each cavity used as the logic basis state  $|0\rangle_L$  to the vacuum state, and the second pair restore the original coherent states.

Figure 3 shows the two-cavity geometric phase gates based on Device B, whose schematic is shown in Fig. 3(a). Besides the transmon qubit simultaneously coupled to both cavities, each cavity also dispersively couples to another ancillary transmon qubit for encoding/decoding and measurement purposes. Figure 3(b) shows the experimental sequence for the process tomography to benchmark the gate performance. In our experiment, the CZ gate is implemented with two different encoding schemes: coherent state encoding  $\{|0\rangle, |2\alpha\rangle\}$  and Fock state encoding  $\{|0\rangle, |1\rangle\}$  for both cavities. The measured Pauli transfer  $R$  matrices of the CZ gates, together with the  $R$  matrix for the ideal CZ gate, are shown in Fig. 3(c). The process  $R$  matrix fidelities,  $F_{CZ,ED}$  ( $F_{ED}$ ), for these two encodings are 0.727 (0.869) and 0.862 (0.905), respectively. We note that for the Fock state encoding the infidelity dominantly comes from the encoding-decoding process; for the coherent state encoding, besides the encoding-decoding error

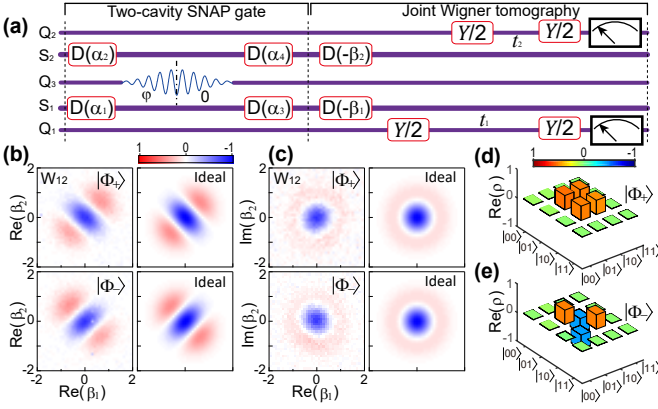


FIG. 4: Two-cavity SNAP gate to create single-photon Bell states  $|\Phi_{\pm}\rangle = (|01\rangle \pm |10\rangle)/\sqrt{2}$ . (a) Experimental sequence, which consists of a conditional  $2\pi$  rotation on the qubit  $Q_3$  and four displacements of the cavity states, followed by joint Wigner tomography measurements. (b) and (c) The measured joint Wigner function  $W_{12}$  of the Bell states  $|\Phi_{+}\rangle$  and  $|\Phi_{-}\rangle$  on the Re-Re and Im-Re planes, respectively. (d) and (e) Real parts of the density matrices of the states  $|\Phi_{+}\rangle$  and  $|\Phi_{-}\rangle$  measured with the decoding and state tomography sequence as shown in Fig. 3(b), respectively. Solid black outlines are for the ideal density matrices. Measured imaginary parts for both states are smaller than 0.04 and not shown. The fidelities for  $|\Phi_{\pm}\rangle$  are 0.957 and 0.930, respectively.

the fidelity loss mainly comes from the Kerr effects that deform the coherent states during the gate operation.

Our approach can also be used to realize a CNOT gate between two cavities. As a particular example, the control cavity  $S_1$  is encoded with Fock states  $\{|0\rangle, |1\rangle\}$  and the target cavity  $S_2$  is encoded with  $\{|0\rangle_L = (|0\rangle + |2\rangle)/\sqrt{2}, |1\rangle_L = (|0\rangle - |2\rangle)/\sqrt{2}\}$ . We note that this gate is equivalent to the CZ gate with the logic basis states of the target qubit encoded in the zero- and two-photon states. The measured Pauli transfer  $R$  matrix of the two-cavity CNOT gate is shown in Fig. 3(d), corresponding to a process  $R$  matrix fidelity,  $F_{\text{CNOT,ED}}(F_{\text{ED}})$ , of 0.829 (0.857).

We finally show that our conditional dynamics can be used to deterministically create high-fidelity single-photon Bell states  $|\Phi_{\pm}\rangle = (|01\rangle \pm |10\rangle)/\sqrt{2}$ . The approach is an extension of the previously reported SNAP operation for universal control of one cavity [17, 18] to two cavities. When combined with the single-cavity SNAP gates, our method can be used to realize arbitrary universal multi-cavity control. The experimental sequence is shown in Fig. 4(a), where a conditional  $2\pi$  rotation on qubit  $Q_3$  is sandwiched in between two pairs of phase-space displacements of the cavities. With help of the two ancillary qubits, joint Wigner tomography of the two cavities is performed and two slice cuts of the measured two-mode Wigner function are shown in Figs. 4(b-c). The density matrices of  $|\Phi_{+}\rangle$  and  $|\Phi_{-}\rangle$ , reconstructed by mapping the state of the two cavities to qubits  $Q_1$  and  $Q_2$  and then jointly measuring the state of these qubits [as in the tomography measurement of Fig. 3(b)], are displayed in Figs. 4(d-e), with state fidelities of 0.957 and 0.930, respectively.

One distinct feature of our gate dynamics is that it is compatible with error correction schemes. For logic qubits whose basis states are encoded in even cat states, the photon-number parity can be used as an error syndrome of the single-photon loss [21–23]. With this encoding, each of the two-qubit logic basis states is composed of four two-mode coherent state components, and a CZ gate can be realized by subsequently performing four conditional phase operations. Each operation inverts the phase of one of the four components forming a specific logic basis state, and can be realized by sandwiching a qubit  $2\pi$  rotation conditional on the cavities' vacuum state between two pairs of phase-space displacements of the cavities. For another kind of error-correctable logic qubits binomially encoded as  $\{|0\rangle_L = (|0\rangle + |4\rangle)/\sqrt{2}, |1\rangle_L = |2\rangle\}$  [45, 46], the CZ gate can be realized by a qubit  $2\pi$  rotation conditional on the joint cavities' state  $|2\rangle|2\rangle$ , enabled with a drive at the qubit's frequency associated with this cavities' state. For our device, the error due to Kerr effects is larger than that caused by single-photon loss. With the improvement of the device design, the Kerr strengths can be significantly mitigated [19]. We plan to design and fabricate a device with improved performance, and demonstrate gates with error-correctable logic qubits.

For a setup with three or more cavities coupled to one common qubit, the qubit  $2\pi$  rotation conditional on all cavities being in the vacuum state directly leads to a phase gate acting on these cavities if the vacuum state in each cavity acts as the logic basis state  $|0\rangle_L$ . This kind of gates is useful for quantum error correction [47] and serves as a central element for implementation of the quantum search algorithm [48]. In addition to implementation of quantum gates, our method can be used for stabilizing the parity of a cat state: When an environmentally-induced parity jump occurs, one can correct for it through the combination of a conditional qubit  $2\pi$  rotation and two displacement operations.

We thank valuable discussions with Chen Wang. This work was supported by National Key Research and Development Program of China No.2017YFA0304303 and the National Natural Science Foundation of China under Grants No.11474177, No. 11874114, No. 11674060, and No. 11875108.

\* Electronic address: zbyang@fzu.edu.cn

† Electronic address: t96034@fzu.edu.cn

‡ Electronic address: luyansun@tsinghua.edu.cn

- [1] J. Anandan, *Nature* **360**, 307 (1992).
- [2] F. Wilczek and A. Shapere, *Geometric Phases in Physics* (WORLD SCIENTIFIC, 1989).
- [3] M. V. Berry, *Proc. R. Soc. Lond.* **392**, 45 (1984).
- [4] G. De Chiara and G. M. Palma, *Phys. Rev. Lett.* **91**, 090404 (2003).
- [5] L. Duan, J. I. Cirac, and P. Zoller, *Science* **292**, 1695 (2001).
- [6] J. A. Jones, V. Vedral, A. Ekert, and G. Castagnoli, *Nature* **403**, 869 (2000).
- [7] R. Tycko, *Phys. Rev. Lett.* **58**, 2281 (1987).

- [8] P. J. Leek, J. M. Fink, A. Blais, R. Bianchetti, M. Göppl, J. M. Gambetta, D. I. Schuster, L. Frunzio, R. J. Schoelkopf, and A. Wallraff, *Science* **318**, 1889 (2007).
- [9] S. Filipp, J. Klepp, Y. Hasegawa, C. Plonka-Spehr, U. Schmidt, P. Geltenbort, and H. Rauch, *Phys. Rev. Lett.* **102**, 030404 (2009).
- [10] M. Pechal, S. Berger, A. A. Abdumalikov, J. M. Fink, J. A. Mlynek, L. Steffen, A. Wallraff, and S. Filipp, *Phys. Rev. Lett.* **108**, 170401 (2012).
- [11] S. Gasparinetti, S. Berger, A. A. Abdumalikov, M. Pechal, S. Filipp, and A. J. Wallraff, *Sci. Adv.* **2**, e1501732 (2016).
- [12] Y. Aharonov and J. Anandan, *Phys. Rev. Lett.* **58**, 1593 (1987).
- [13] J. Samuel and R. Bhandari, *Phys. Rev. Lett.* **60**, 2339 (1988).
- [14] S.-B. Zheng, *Phys. Rev. A* **70**, 052320 (2004).
- [15] D. Leibfried, B. DeMarco, V. Meyer, D. Lucas, M. Barrett, J. Britton, W. M. Itano, B. Jelenković, C. Langer, T. Rosenband, et al., *Nature* **422**, 412 (2003).
- [16] C. Song, S.-B. Zheng, P. Zhang, K. Xu, L. Zhang, Q. Guo, W. Liu, D. Xu, H. Deng, K. Huang, et al., *Nat. Commun.* **8**, 1061 (2017).
- [17] S. Krastanov, V. V. Albert, C. Shen, C.-L. Zou, R. W. Heeres, B. Vlastakis, R. J. Schoelkopf, and L. Jiang, *Phys. Rev. A* **92**, 040303 (2015).
- [18] R. W. Heeres, B. Vlastakis, E. Holland, S. Krastanov, V. V. Albert, L. Frunzio, L. Jiang, and R. J. Schoelkopf, *Phys. Rev. Lett.* **115**, 137002 (2015).
- [19] S. Rosenblum, Y. Y. Gao, P. Reinhold, C. Wang, C. J. Axline, L. Frunzio, S. M. Girvin, L. Jiang, M. Mirrahimi, M. H. Devoret, et al., *Nat. Commun.* **9**, 652 (2018).
- [20] S. Deléglise, I. Dotsenko, C. Sayrin, J. Bernu, M. Brune, J. M. Raimond, and S. Haroche, *Nature* **455**, 510 (2008).
- [21] Z. Leghtas, G. Kirchmair, B. Vlastakis, R. J. Schoelkopf, M. H. Devoret, and M. Mirrahimi, *Phys. Rev. Lett.* **111**, 120501 (2013).
- [22] M. Mirrahimi, Z. Leghtas, V. V. Albert, S. Touzard, R. J. Schoelkopf, L. Jiang, and M. H. Devoret, *New J. Phys.* **16**, 045014 (2014).
- [23] N. Ofek, A. Petrenko, R. Heeres, P. Reinhold, Z. Leghtas, B. Vlastakis, Y. Liu, L. Frunzio, S. M. Girvin, L. Jiang, et al., *Nature* **536**, 441 (2016).
- [24] R. Heeres, P. Reinhold, N. Ofek, L. Frunzio, L. Jiang, M. H. Devoret, and R. J. Schoelkopf, *Nat. Commun.* **8**, 94 (2017).
- [25] L. Sun, A. Petrenko, Z. Leghtas, B. Vlastakis, G. Kirchmair, K. M. Sliwa, A. Narla, M. Hatridge, S. Shankar, J. Blumoff, et al., *Nature* **511**, 444 (2014).
- [26] A. Wallraff, D. I. Schuster, A. Blais, L. Frunzio, R.-S. Huang, J. Majer, S. Kumar, S. M. Girvin, and R. J. Schoelkopf, *Nature* **431**, 162 (2004).
- [27] J. Clarke and F. K. Wilhelm, *Nature* **453**, 1031 (2008).
- [28] J. Q. You and F. Nori, *Nature* **474**, 589 (2011).
- [29] M. H. Devoret and R. J. Schoelkopf, *Science* **339**, 1169 (2013).
- [30] X. Gu, A. F. Kockum, A. Miranowicz, Y. X. Liu, and F. Nori, *Phys. Rep.* **718-719**, 1 (2017).
- [31] H. Paik, D. I. Schuster, L. S. Bishop, G. Kirchmair, G. Catelani, A. P. Sears, B. R. Johnson, M. J. Reagor, L. Frunzio, L. I. Glazman, et al., *Phys. Rev. Lett.* **107**, 240501 (2011).
- [32] G. Kirchmair, B. Vlastakis, Z. Leghtas, S. E. Nigg, H. Paik, E. Ginossar, M. Mirrahimi, L. Frunzio, S. M. Girvin, and R. J. Schoelkopf, *Nature* **495**, 205 (2013).
- [33] B. Vlastakis, G. Kirchmair, Z. Leghtas, S. E. Nigg, L. Frunzio, S. M. Girvin, M. Mirrahimi, M. H. Devoret, and R. J. Schoelkopf, *Science* **342**, 607 (2013).
- [34] K. Liu, Y. Xu, W. Wang, S.-B. Zheng, T. Roy, S. Kundu, M. Chand, A. Ranadive, R. Vijay, Y. Song, et al., *Sci. Adv.* **3**, e1603159 (2017).
- [35] W. Wang, L. Hu, Y. Xu, K. Liu, Y. Ma, S.-B. Zheng, R. Vijay, Y. P. Song, L.-M. Duan, and L. Sun, *Phys. Rev. Lett.* **118**, 223604 (2017).
- [36] Y. Xu, W. Cai, Y. Ma, X. Mu, L. Hu, T. Chen, H. Wang, Y. P. Song, Z.-Y. Xue, Z.-q. Yin, et al., *Phys. Rev. Lett.* **121**, 110501 (2018).
- [37] M. Reagor, W. Pfaff, C. Axline, R. W. Heeres, N. Ofek, K. Sliwa, E. Holland, C. Wang, J. Blumoff, K. Chou, et al., *Phys. Rev. B* **94**, 014506 (2016).
- [38] C. Axline, M. Reagor, R. Heeres, P. Reinhold, C. Wang, K. Shain, W. Pfaff, Y. Chu, L. Frunzio, and R. J. Schoelkopf, *Appl. Phys. Lett.* **109**, 042601 (2016).
- [39] Supplementary Materials.
- [40] N. Khaneja, T. Reiss, C. Kehlet, T. Schulte-Herbrüggen, and S. J. Glaser, *Journal of Magnetic Resonance* **172**, 296 (2005).
- [41] P. de Fouquieres, S. Schirmer, S. Glaser, and I. Kuprov, *Journal of Magnetic Resonance* **212**, 412 (2011).
- [42] J. M. Chow, J. M. Gambetta, A. D. Córcoles, S. T. Merkel, J. A. Smolin, C. Rigetti, S. Poletto, G. A. Keefe, M. B. Rothwell, J. R. Rozen, et al., *Phys. Rev. Lett.* **109**, 060501 (2012).
- [43] C. Wang, Y. Y. Gao, P. Reinhold, R. W. Heeres, N. Ofek, K. Chou, C. Axline, M. Reagor, J. Blumoff, K. Sliwa, et al., *Science* **352**, 1087 (2016).
- [44] Y. Y. Gao, B. J. Lester, K. Chou, L. Frunzio, M. H. Devoret, L. Jiang, S. M. Girvin, and R. J. Schoelkopf, arXiv:1806.07401 (2018).
- [45] M. H. Michael, M. Silveri, R. T. Brierley, V. V. Albert, J. Salmilehto, L. Jiang, and S. M. Girvin, *Phys. Rev. X* **6**, 031006 (2016).
- [46] L. Hu, Y. Ma, W. Cai, X. Mu, Y. Xu, W. Wang, Y. Wu, H. Wang, Y. Song, C. Zou, et al., arXiv:1805.09072 (2018).
- [47] M. D. Reed, L. DiCarlo, S. E. Nigg, L. Sun, L. Frunzio, S. M. Girvin, and R. J. Schoelkopf, *Nature* **482**, 382 (2012).
- [48] M. A. Nielsen and I. L. Chuang, *Quantum Computation and Quantum Information* (Cambridge Univ. Press, 2000).

# Supplementary Material for “Geometrically manipulating photonic Schrödinger cat states and realizing cavity phase gates”

Y. Xu,<sup>1</sup> W. Cai,<sup>1</sup> Y. Ma,<sup>1</sup> X. Mu,<sup>1</sup> W. Dai,<sup>1</sup> W. Wang,<sup>1</sup> L. Hu,<sup>1</sup> X. Li,<sup>1</sup> J. Han,<sup>1</sup>  
H. Wang,<sup>1</sup> Y. P. Song,<sup>1</sup> Zhen-Biao Yang,<sup>2,\*</sup> Shi-Biao Zheng,<sup>2,†</sup> and L. Sun<sup>1,‡</sup>

<sup>1</sup>Center for Quantum Information, Institute for Interdisciplinary Information Sciences, Tsinghua University, Beijing 100084, China

<sup>2</sup>Fujian Key Laboratory of Quantum Information and Quantum Optics,

College of Physics and Information Engineering, Fuzhou University, Fuzhou, Fujian 350116, China

## I. EXPERIMENTAL DEVICE AND SETUP

The single-cavity geometric phase gates are performed on Device A, which consists of two transmon qubits simultaneously dispersively coupled to two three-dimensional (3D) cavities [1–5]. Details of the device parameters and architecture setup are described in Ref. [6]. Here we only describe Device B in detail.

Device B with a circuit quantum electrodynamics (cQED) architecture contains two 3D coaxial stub cavities ( $S_1$  and  $S_2$ ), three superconducting transmon qubits ( $Q_1$ ,  $Q_2$ , and  $Q_3$ ), and three stripline readout resonators ( $R_1$ ,  $R_2$ , and  $R_3$ ). The 3D view of Device B is shown in Fig. 3(a) of the main text and the optical image is shown in Fig. S1. The device is machined from a block of high-purity (5N5) aluminum and is chemically etched to improve the surface quality [7]. The two coaxial cavities are 3D  $\lambda/4$  transmission line resonators [8–10] with a center conductor of 3.3 mm in diameter and a cylindrical wall of 9.6 mm in diameter. The fundamental mode frequencies are mainly determined by the heights of the center stubs, 9.8 mm and 10.8 mm for  $S_1$  and  $S_2$  respectively. There are three horizontal tunnels housing three individual sapphire chips with patterned transmon qubits to couple to the two cavity modes. Qubit  $Q_3$  on the middle chip is designed with three antenna pads to couple to the two coaxial cavity modes and one stripline readout mode, respectively. Each of the other two

ancillary qubits ( $Q_1$  and  $Q_2$ ) only has two antenna pads to couple to the corresponding cavity mode and individual stripline readout resonator. Each stripline readout resonator is formed by the metal wall of the tunnel and an aluminum strip simultaneously patterned on the same chip with the transmon qubit through a standard double-angle evaporation process after a single electron-beam lithography step.

The device is anchored to the mixing chamber of a cryogenic dilution refrigerator which is cooled down to  $T \approx 10$  mK. An additional magnetic shield covering the device is used to provide a clean electromagnetic environment. Attenuators and low-pass filters are used on the microwave lines to reduce the radiation noises of the signals. All the qubit and cavity drives are generated by IQ modulations with two analog channels of a Tektronix AWG5014C and an IQ mixer. The cavity states are initialized with the help of the ancillary qubits following the gradient ascent pulse engineering (GRAPE) technique [11, 12]. The qubit control pulses have a truncated Gaussian envelope with a width of  $4\sigma = 20$  ns. With the technique of “derivative removal by adiabatic gate” (DRAG) to remove the leakage and phase errors of the drive pulses [13, 14], the single qubit gates, characterized by the randomized benchmarking method [15–19], result in an average fidelity of 0.9990, 0.9986, and 0.9992 for the three qubits respectively. The three qubits can be simultaneously measured with three individual readout control signals generated with different modulations of the same local oscillator (LO). The readout signals are first amplified by quantum limited amplifiers at base temperature. We use two separate Josephson parametric amplifiers (JPA) for  $Q_1$  and  $Q_2$ , and a Josephson parametric converter (JPC) for  $Q_3$ . Each readout signal is further amplified by a high electron mobility transistor (HEMT) at 4K stage and a standard commercial RF amplifier at room temperature. Finally, the three readout signals are combined together and mixed down with the LO. After being digitized and recorded by the analog-to-digital converters (ADC), the three readout signals can be distinguished through demodulations with different frequencies. The schematic of the full wiring of the experimental setup is shown in Fig. S2.

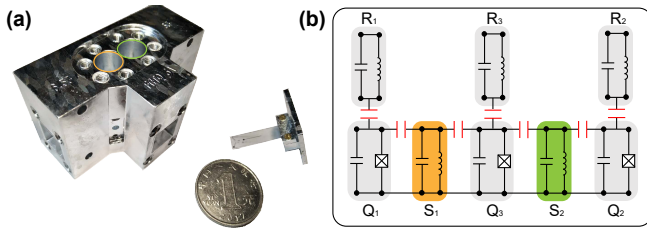


FIG. S1: (a) Optical image of Device B. The device is machined from a block of high-purity (5N5) aluminum and is chemically etched. It consists of two coaxial stub cavities and three transmon qubits on different individual sapphire chips in three separate horizontal tunnels. Each qubit also couples to an individual stripline readout resonator. (b) Schematic of the effective circuit of Device B.

## II. SYSTEM HAMILTONIAN

The three transmon qubits are dispersively coupled to the corresponding 3D cavity modes. Each transmon has a large anharmonicity and is considered as a two-level artificial atom, while each cavity mode is considered as a harmonic oscillator. Thus, the whole system can be described by the following

\*Electronic address: zbyang@fzu.edu.cn

†Electronic address: t96034@fzu.edu.cn

‡Electronic address: luyansun@tsinghua.edu.cn

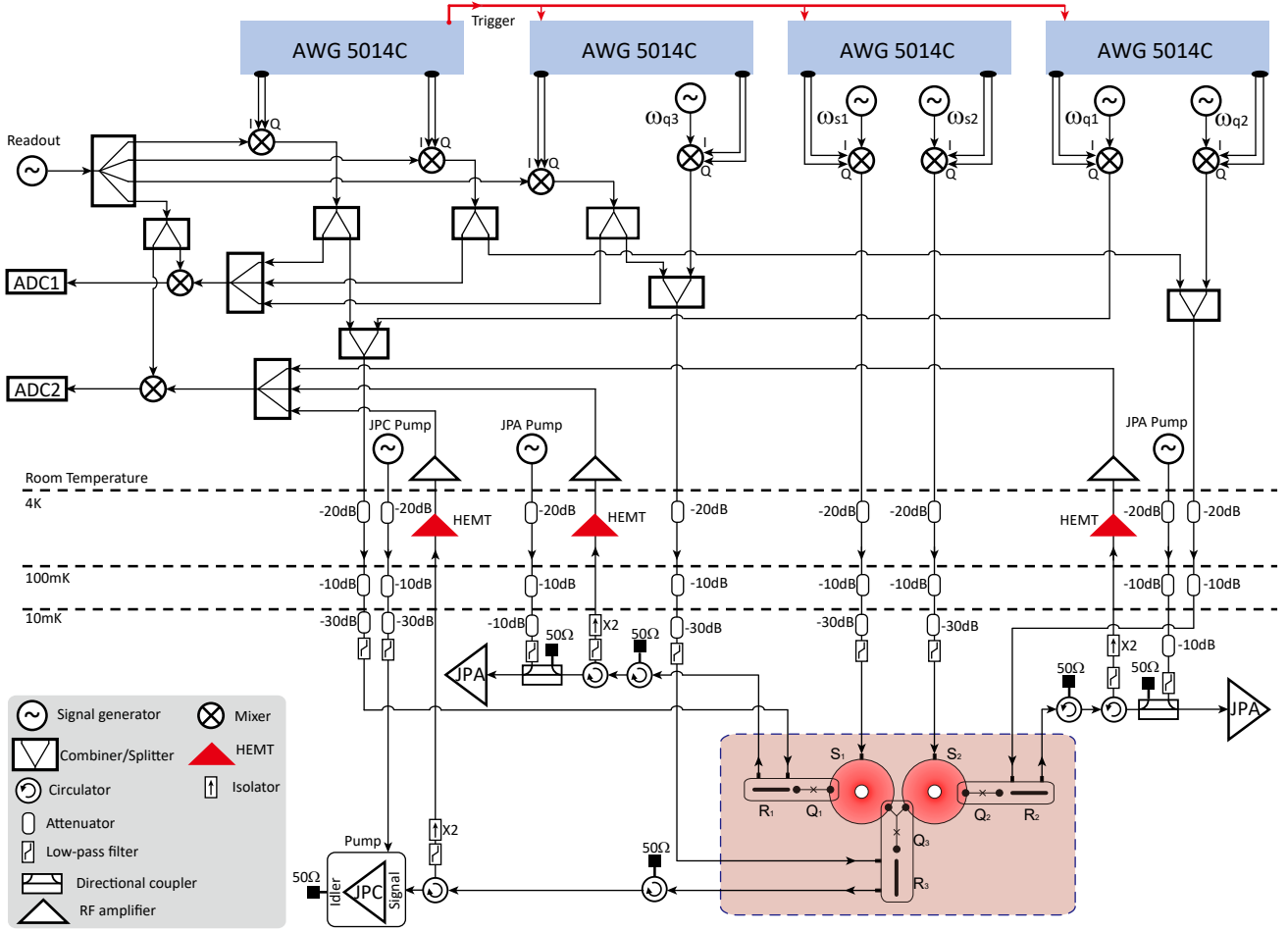


FIG. S2: Schematic of the full wiring of the experimental setup.

Hamiltonian

$$\begin{aligned}
 \mathcal{H}/\hbar = & \sum_{i=1}^3 \omega_{ri} a_{ri}^\dagger a_{ri} + \sum_{i=1}^3 \omega_{qi} |e_i\rangle \langle e_i| + \sum_{i=1}^2 \omega_{si} a_{si}^\dagger a_{si} \\
 & - \sum_{i=1}^3 \chi_{rqi} |e_i\rangle \langle e_i| a_{ri}^\dagger a_{ri} \\
 & - \chi_{s1q1} |e_1\rangle \langle e_1| a_{s1}^\dagger a_{s1} - \chi_{s1q3} |e_3\rangle \langle e_3| a_{s1}^\dagger a_{s1} \\
 & - \chi_{s2q2} |e_2\rangle \langle e_2| a_{s2}^\dagger a_{s2} - \chi_{s2q3} |e_3\rangle \langle e_3| a_{s2}^\dagger a_{s2} \\
 & - \sum_{i=1}^2 \frac{K_{si}}{2} a_{si}^\dagger a_{si}^\dagger a_{si} a_{si} - \chi_{s1s2} a_{s1}^\dagger a_{s1} a_{s2}^\dagger a_{s2}, \quad (1)
 \end{aligned}$$

where  $\omega_{ri}$  is the readout resonator frequency of the  $i$ -th qubit with the corresponding ladder operators  $a_{ri}$  and  $a_{ri}^\dagger$ ;  $\omega_{si}$  are the resonant frequency of the  $i$ -th storage cavity with the corresponding ladder operators  $a_{si}$  and  $a_{si}^\dagger$ ;  $\omega_{qi}$  is the transition frequency between the lowest two energy levels of the  $i$ -th qubit;  $\chi_{rqi}$  is the dispersive interaction between the  $i$ -th qubit and its corresponding readout resonator;  $\chi_{s1q1}$ ,  $\chi_{s1q3}$ ,  $\chi_{s2q2}$ , and  $\chi_{s2q3}$  are the dispersive interactions between the three qubits and the two storage cavity modes;  $K_{si}$  is the self-Kerr of the  $i$ -th

storage cavity; and  $\chi_{s1s2}$  is the cross-Kerr of the two storage cavities. All the relevant parameters in the Hamiltonian are experimentally measured and listed in Table S1.

The coherence properties of the qubits and the cavity modes are also experimentally characterized with the standard cQED measurements. In particular, the coherence times  $T_1$  and  $T_2^*$  of the storage cavities are measured through the relaxing of the Fock state  $|1\rangle$  and the dephasing of the superposition state  $(|0\rangle + |1\rangle)/\sqrt{2}$ , respectively [8]. Both initial states are generated with the selective number-dependent arbitrary phase (SNAP) gates [20]. All the results are listed in Table S2.

### III. SIMULTANEOUS READOUT

In our experiment, each transmon qubit is connected to a quantum limited amplifier for fast high-fidelity single-shot readouts. The independence of the drives and measurements on them can be verified by simultaneous readouts of the two ancillary qubits, and the results are shown in Fig. S3.

In order to calibrate the three-qubit readout error, we prepare the system in each computational basis state and simultaneously measure the assignment probability

TABLE S1: Measured Hamiltonian parameters.

Modes	Frequency (GHz)	Nonlinear terms: $\chi_{ij}/2\pi$ (MHz)				
		$S_1$	$S_2$	$Q_1$	$Q_2$	$Q_3$
$S_1$	6.586	0.009	0.017	1.828	-	1.247
$S_2$	6.050	0.017	0.029	-	2.800	2.368
$Q_1$	6.082	1.828	-	252	-	-
$Q_2$	5.207	-	2.800	-	207	-
$Q_3$	5.659	1.247	2.368	-	-	151
$R_1$	8.892	-	-	1.6	-	-
$R_2$	8.801	-	-	-	2.0	-
$R_3$	8.953	-	-	-	-	1.6

TABLE S2: Coherence properties of the system.

Modes	$T_1$	$T_2^*$	$T_2^{\text{Echo}}$
$S_1$	596 $\mu\text{s}$	213 $\mu\text{s}$	-
$S_2$	595 $\mu\text{s}$	336 $\mu\text{s}$	-
$Q_1$	33.6 $\mu\text{s}$	18.6 $\mu\text{s}$	56.0 $\mu\text{s}$
$Q_2$	9.7 $\mu\text{s}$	5.3 $\mu\text{s}$	19.1 $\mu\text{s}$
$Q_3$	35.3 $\mu\text{s}$	15.0 $\mu\text{s}$	26.1 $\mu\text{s}$
$R_1$	63 ns	-	-
$R_2$	55 ns	-	-
$R_3$	116 ns	-	-

TABLE S3: Three-qubit simultaneous readout assignment probability matrix  $\mathcal{R}$ . Each column represents the three-qubit measurement probabilities after preparing the qubits in the corresponding computational basis state.

	$ ggg\rangle$	$ gge\rangle$	$ geg\rangle$	$ gee\rangle$	$ egg\rangle$	$ ege\rangle$	$ eeg\rangle$	$ eee\rangle$
000	95.2	4.0	7.8	0.3	5.9	0.2	0.5	0.0
001	0.8	92.4	0.1	7.5	0.1	4.8	0.0	0.4
010	2.1	0.1	89.9	3.7	0.1	0.0	6.3	0.2
011	0.0	2.0	0.8	87.1	0.0	0.1	0.1	4.4
100	1.8	0.1	0.1	0.0	91.2	3.6	7.3	0.3
101	0.0	1.5	0.0	0.1	0.7	89.3	0.1	7.2
110	0.0	0.0	1.4	0.0	1.9	0.1	85.0	3.4
111	0.0	0.0	0.0	1.2	0.0	1.9	0.8	84.0

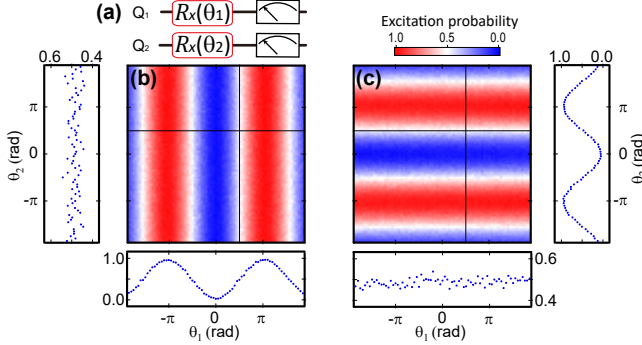


FIG. S3: Simultaneous Rabi experiments on the two ancillary qubits. (a) The experimental pulse sequence, where the two ancillary qubits are rotated along  $x$  axis with independent angles  $\theta_1$  and  $\theta_2$ , respectively, followed by simultaneous measurements on both of them. The measured excitation probabilities of qubits  $Q_1$  and  $Q_2$  as a function of the rotation angles  $\theta_1$  and  $\theta_2$  are shown in (b) and (c), respectively. The horizon and vertical cuts are also shown accordingly.

$\vec{p} = (p_{000}, p_{001}, p_{010}, p_{011}, p_{100}, p_{101}, p_{110}, p_{111})^T$  of the three qubits. By repeating the experiments for all the three-qubit computational basis states, we obtain the  $8 \times 8$  readout matrix  $\mathcal{R}$  as shown in Table S3. We then can correct the readout errors by multiplying the inverse of the readout matrix  $\mathcal{R}$  with the measured probability  $\vec{p}$ , such that  $\vec{p}_{\text{corr}} = \mathcal{R}^{-1} \cdot \vec{p}$  represents the real occupation probabilities of the eight computational basis states. For all the two-cavity experimental data shown in the main text, we have corrected the readout errors with this method.

#### IV. QUANTUM PROCESS TOMOGRAPHY

Both the single-cavity and two-cavity phase gates are characterized with full quantum process tomography (QPT) [21]. To make the preparation and characterization easier, we instead use the adjacent ancillary qubits to facilitate the encoding and decoding processes of the cavity states. The encoding and decoding processes are realized by quantum optimal control with the GRAPE technique. The final state is reconstructed with pre-rotations  $\{I, X_{\pi/2}, Y_{\pi/2}, X_{\pi}\}$  on each ancillary qubit before measurements. The density matrix is then reconstructed by the maximum likelihood estimation method [22].

Here, we use the Pauli transfer matrix  $R$  to represent the quantum process, which is visually efficient and informative [23]. In order to characterize the quantum process, before the encoding process we use initial states  $\{|g\rangle, |e\rangle, (|g\rangle + |e\rangle)/\sqrt{2}, (|g\rangle - |e\rangle)/\sqrt{2}\}$  of the ancillary qubit for the single-cavity gates and  $\{|g\rangle, |e\rangle, (|g\rangle + |e\rangle)/\sqrt{2}, (|g\rangle - |e\rangle)/\sqrt{2}\}^{\otimes 2}$  of the ancillary qubits for the two-cavity gates. The  $R$  matrix maps the input state vector  $\vec{p}_{\text{in}}$  with the output state vector  $\vec{p}_{\text{out}}$  by  $\vec{p}_{\text{out}} = R \cdot \vec{p}_{\text{in}}$ . The process fidelity is calculated from the measured  $R$  matrix with

$$F = \frac{\text{Tr}(R^\dagger R_{\text{ideal}})/d + 1}{d + 1}, \quad (2)$$

where  $R_{\text{ideal}}$  is for a perfect process,  $d = 2n$ , and  $n$  is the number of cavities.

## V. JOINT WIGNER TOMOGRAPHY

We verify the quantum entanglement of the two-cavity states with the joint Wigner tomography [9], which is a measurement of the displaced joint photon number parity  $P_J(\beta_1, \beta_2)$  of the two cavities. We simultaneously map the parity of each cavity to its adjacent ancillary qubit. The single-shot readout of each qubit allows us to extract the displaced joint parity  $P_J(\beta_1, \beta_2) = P_1(\beta_1)P_2(\beta_2)$  by multiplying the two individually displaced cavity parities  $P_1(\beta_1)$  and  $P_2(\beta_2)$ .

The realized two-cavity entangled gates can be effectively used for generating entangled two-cavity states. We use the joint Wigner tomography to characterize these entangled cavity states. The joint Wigner cuts of two example entangled cavity states  $|\psi_1\rangle = (|00\rangle + e^{i\varphi_1}|01\rangle + e^{i\varphi_2}|10\rangle + e^{i(\varphi_1+\varphi_2+\pi)}|11\rangle)/2$  and  $|\psi_2\rangle = (|00\rangle + e^{i\varphi_3}|02\rangle + e^{i\varphi_4}|10\rangle + e^{i(\varphi_3+\varphi_4+\pi)}|12\rangle)/2$  are shown in Fig. S4. The single-cavity phases  $\varphi_1 = -69$  deg,  $\varphi_2 = -143$  deg,  $\varphi_3 = -62$  deg, and  $\varphi_4 = -164$  deg can be eliminated with the realized single-cavity geometric phase gates. In our experiment, these phases are included in the decoding pulses.

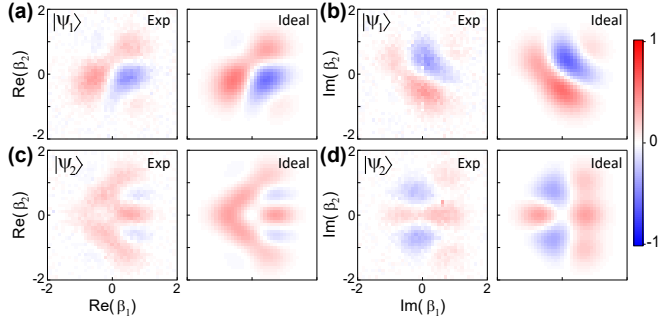


FIG. S4: Joint Wigner functions in the Re-Re plane (a, c) and Im-Im plane (b, d) for the entangled cavity states  $|\psi_1\rangle$  (a, b) and  $|\psi_2\rangle$  (c, d), respectively.

## VI. TWO-CAVITY SNAP GATES

The single-photon Bell states  $|\Phi_{\pm}\rangle = (|01\rangle \pm |10\rangle)/\sqrt{2}$  are deterministically generated with the two-cavity SNAP gates, where the four displacement amplitudes,  $\alpha_1 = \mp 0.8082$ ,  $\alpha_2 = -0.8082$ ,  $\alpha_3 = \pm 0.4103$ , and  $\alpha_4 = 0.4103$ , are calculated from numerical simulation and further optimized in experiment in order to achieve higher state fidelities. The joint Wigner functions of these states have been shown in the main text. Single-cavity Wigner functions on storage cavities  $S_1$  and  $S_2$  have also been performed and are shown in Fig. S5. The measured single-cavity Wigner functions indicate mixed states of Fock states  $|0\rangle$  and  $|1\rangle$  as expected. Therefore, these results manifest that the generated two-cavity states are no longer separable and the individual cavity measurement destroys the coherence between them.

## VII. GATE ERROR ANALYSIS

For the single-cavity geometric phase gates with the coherent state encoding, the cavity state preparation and measurement errors are mainly due to the ancillary qubit decoherence and the imperfection of the GRAPE pulses. These errors can be estimated from the measured process fidelity  $F_{\text{ED}} = 0.969$  for the process with the encoding and decoding only. The difference between the process fidelities  $F_{\text{ED}}$  and  $F_{\text{Gate\_ED}}$  gives the intrinsic infidelity ( $\sim 0.012$ ) of the phase gates, which comes from two main error sources. One is the relaxation of qubit  $Q_1$  during the gate operation and the other is the imperfect selectivity of the qubit conditional rotation. Each contributes an infidelity of about 0.01 to the phase gates. Besides, the deterministic small deformation and rotation of the cavity states due to the non-negligible self-Kerr need to be taken into account and have been included in the decoding pulses.

For the two-cavity geometric phase gates, all the GRAPE pulses for the encoding and decoding processes in the numerical optimizations include only the  $\chi$  interaction between the cavity and its corresponding ancillary transmon qubit, while the cross-Kerr interaction ( $\chi_{s_1s_2}/2\pi = 29$  kHz) between the two cavities is excluded. In our experiment,  $F_{\text{ED}} \sim 0.90$  is mainly due to the ancillary qubit decoherence and the imperfection of the GRAPE pulses. For the coherent state encoding, the cross-Kerr interaction deforms the two-cavity states greatly during the gate, therefore, introduces not only errors for the gate operation, but also errors in the subsequent decoding process. These two combined errors contribute dominantly to the difference between  $F_{\text{Gate\_ED}}$  and  $F_{\text{ED}}$  ( $\sim 0.14$ ). The other errors include the relaxation of the qubits during the gate operation and the imperfect selectivity of the qubit conditional rotation (infidelity of  $\sim 0.01$  for each). For the Fock state encoding, the cross-Kerr interaction only induces an additional deterministic entangled phase of the two-cavity states and has been eliminated in the geometric phase gate, resulting in a much higher gate fidelity ( $\sim 0.957$ ).

For the single-photon Bell states  $|\Phi_{\pm}\rangle$  generated with the two-cavity SNAP gate, the measured state fidelities are mainly limited by the imperfection of the decoding pulses (infidelity of  $\sim 0.045$ ), as well as the qubit relaxation and the imperfect selectivity of the qubit rotation (infidelity of  $\sim 0.01$  for each).

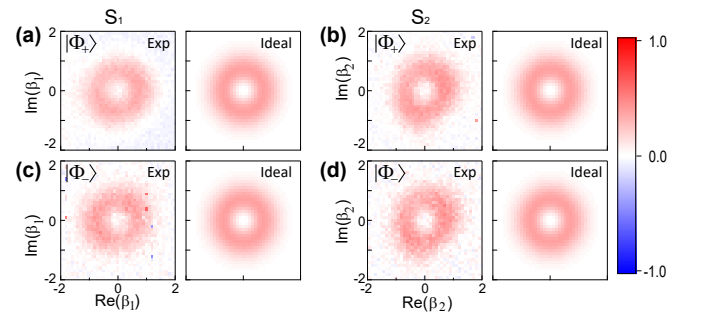


FIG. S5: Single-cavity Wigner functions of the entangled states  $|\Phi_+\rangle$  (a, b) and  $|\Phi_-\rangle$  (c, d), respectively, measured from the storage cavities  $S_1$  (a, c) and  $S_2$  (b, d).

- 
- [1] H. Paik, D. I. Schuster, L. S. Bishop, G. Kirchmair, G. Catelani, A. P. Sears, B. R. Johnson, M. J. Reagor, L. Frunzio, L. I. Glazman, et al., *Phys. Rev. Lett.* **107**, 240501 (2011).
- [2] B. Vlastakis, G. Kirchmair, Z. Leghtas, S. E. Nigg, L. Frunzio, S. M. Girvin, M. Mirrahimi, M. H. Devoret, and R. J. Schoelkopf, *Science* **342**, 607 (2013).
- [3] K. Liu, Y. Xu, W. Wang, S.-B. Zheng, T. Roy, S. Kundu, M. Chand, A. Ranadive, R. Vijay, Y. Song, et al., *Sci. Adv.* **3**, e1603159 (2017).
- [4] W. Wang, L. Hu, Y. Xu, K. Liu, Y. Ma, S.-B. Zheng, R. Vijay, Y. P. Song, L.-M. Duan, and L. Sun, *Phys. Rev. Lett.* **118**, 223604 (2017).
- [5] L. Hu, Y. Ma, W. Cai, X. Mu, Y. Xu, W. Wang, Y. Wu, H. Wang, Y. Song, C. Zou, et al., arXiv:1805.09072 (2018).
- [6] Y. Xu, W. Cai, Y. Ma, X. Mu, L. Hu, T. Chen, H. Wang, Y. P. Song, Z.-Y. Xue, Z.-q. Yin, et al., *Phys. Rev. Lett.* **121**, 110501 (2018).
- [7] M. Reagor, H. Paik, G. Catelani, L. Sun, C. Axline, E. Holland, I. M. Pop, N. A. Masluk, T. Brecht, L. Frunzio, et al., *Appl. Phys. Lett.* **102**, 192604 (2013).
- [8] M. Reagor, W. Pfaff, C. Axline, R. W. Heeres, N. Ofek, K. Sliwa, E. Holland, C. Wang, J. Blumoff, K. Chou, et al., *Phys. Rev. B* **94**, 014506 (2016).
- [9] C. Wang, Y. Y. Gao, P. Reinhold, R. W. Heeres, N. Ofek, K. Chou, C. Axline, M. Reagor, J. Blumoff, K. Sliwa, et al., *Science* **352**, 1087 (2016).
- [10] Y. Y. Gao, B. J. Lester, K. Chou, L. Frunzio, M. H. Devoret, L. Jiang, S. M. Girvin, and R. J. Schoelkopf, arXiv:1806.07401 (2018).
- [11] N. Khaneja, T. Reiss, C. Kehlet, T. Schulte-Herbrüggen, and S. J. Glaser, *Journal of Magnetic Resonance* **172**, 296 (2005).
- [12] P. de Fouquieres, S. Schirmer, S. Glaser, and I. Kuprov, *Journal of Magnetic Resonance* **212**, 412 (2011).
- [13] F. Motzoi, J. M. Gambetta, P. Rebentrost, and F. K. Wilhelm, *Phys. Rev. Lett.* **103**, 110501 (2009).
- [14] J. M. Gambetta, F. Motzoi, S. T. Merkel, and F. K. Wilhelm, *Phys. Rev. A* **83**, 012308 (2011).
- [15] E. Knill, D. Leibfried, R. Reichle, J. Britton, R. B. Blakestad, J. D. Jost, C. Langer, R. Ozeri, S. Seidelin, and D. J. Wineland, *Phys. Rev. A* **77**, 012307 (2008).
- [16] J. M. Chow, J. M. Gambetta, L. Tornberg, J. Koch, L. S. Bishop, A. A. Houck, B. R. Johnson, L. Frunzio, S. M. Girvin, and R. J. Schoelkopf, *Phys. Rev. Lett.* **102**, 090502 (2009).
- [17] E. Magesan, J. M. Gambetta, B. R. Johnson, C. A. Ryan, J. M. Chow, S. T. Merkel, M. P. da Silva, G. A. Keefe, M. B. Rothwell, T. A. Ohki, et al., *Phys. Rev. Lett.* **109**, 080505 (2012).
- [18] E. Magesan, J. M. Gambetta, and J. Emerson, *Phys. Rev. Lett.* **106**, 180504 (2011).
- [19] R. Barends, J. Kelly, A. Megrant, A. Veitia, D. Sank, E. Jeffrey, T. C. White, J. Mutus, A. G. Fowler, B. Campbell, et al., *Nature* **508**, 500 (2014).
- [20] R. W. Heeres, B. Vlastakis, E. Holland, S. Krastanov, V. V. Albert, L. Frunzio, L. Jiang, and R. J. Schoelkopf, *Phys. Rev. Lett.* **115**, 137002 (2015).
- [21] M. A. Nielsen and I. L. Chuang, *Quantum Computation and Quantum Information* (Cambridge Univ. Press, 2000).
- [22] D. F. V. James, P. G. Kwiat, W. J. Munro, and A. G. White, *Phys. Rev. A* **64**, 052312 (2001).
- [23] J. M. Chow, J. M. Gambetta, A. D. Córcoles, S. T. Merkel, J. A. Smolin, C. Rigetti, S. Poletto, G. A. Keefe, M. B. Rothwell, J. R. Rozen, et al., *Phys. Rev. Lett.* **109**, 060501 (2012).